

UC Irvine

UC Irvine Previously Published Works

Title

Modelling infrared temperature measurements: implications for laser irradiation and cryogen cooling studies

Permalink

<https://escholarship.org/uc/item/2qg3x11t>

Journal

Physics in Medicine and Biology, 45(2)

ISSN

0031-9155

Authors

Choi, Bernard
Pearce, John A
Welch, Ashley J

Publication Date

2000-02-01

DOI

10.1088/0031-9155/45/2/319

Copyright Information

This work is made available under the terms of a Creative Commons Attribution License, available at <https://creativecommons.org/licenses/by/4.0/>

Peer reviewed

Modelling infrared temperature measurements: implications for laser irradiation and cryogen cooling studies

Bernard Choi, John A Pearce and Ashley J Welch

The University of Texas at Austin Biomedical Engineering Program, Austin, TX 78712-1084, USA

E-mail: berniec@mail.utexas.edu, jpearce@mail.utexas.edu and welch@mail.utexas.edu

Received 25 August 1999

Abstract. The use of thermographic techniques has increased as infrared detector technology has evolved and improved. For laser–tissue interactions, thermal cameras have been used to monitor the thermal response of tissue to pulsed and continuous wave irradiation. It is important to note that the temperature indicated by the thermal camera may not be equal to the actual surface temperature. It is crucial to understand the limitations of using thermal cameras to measure temperature during laser irradiation of tissue.

The goal of this study was to demonstrate the potential difference between measured and actual surface temperatures in a quantitative fashion using a 1D finite difference model. Three ablation models and one cryogen spray cooling simulation were adapted from the literature, and predictions of radiometric temperature measurements were calculated. In general, (a) steep superficial temperature gradients, with a surface peak, resulted in an underestimation of the actual surface temperature, (b) steep superficial temperature gradients, with a subsurface peak, resulted in an overestimation, and (c) small gradients led to a relatively accurate temperature estimate.

1. Introduction

Contact temperature measurement devices provide a relatively inexpensive method of measuring the temperature of an object. Thermistors and thermocouples are among the more popular sensors used to monitor a wide variety of situations. During laser irradiation of tissue, these measurement tools have several limitations (Valvano and Pearce 1995): (a) a trade-off commonly exists between the temporal response and the fragility of the device; (b) the thermal properties of the probe are not the same as those of biological media, resulting in aberrations in the local thermal field; (c) the devices absorb incident laser radiation, causing an error in the temperature measurement; (d) temperatures can only be measured at a single point; and (e) high temperature gradients around the probe result in an averaging effect on the temperature measurement.

Infrared (IR) temperature measurements during laser irradiation of biological media have been performed in a number of recent studies (Jansen *et al* 1993, LeCarpentier *et al* 1993, Pearce *et al* 1986, Pfefer *et al* 1999, Small *et al* 1997, Torres *et al* 1990a, b, Welch *et al* 1987, Anvari *et al* 1998). Although IR detectors are typically more expensive than contact temperature probes, and cryogen or thermoelectric cooling is usually required to increase the signal-to-noise ratio to an acceptable level, these devices have several important advantages. The most obvious, and maybe the most important, is that they operate in a

non-contact mode. The response time of these detectors is on the order of microseconds or less (Torres *et al* 1990c). A single detector can cover a large range of temperatures without encountering problems with saturation. Focal plane arrays and flying spot scanners provide 2D thermal images; thus, a radiometric temperature map can be obtained at high frame rates (≥ 30 frames/s).

The advantages of IR detectors over contact temperature probes have resulted in their increased usage and popularity in a wide variety of applications: military, industrial, firefighting, automotive safety, security and medical diagnostics. However, one characteristic of IR detection that is not taken into account is that superficial thermal gradients may result in a discrepancy between the measured radiometric temperature and the actual surface temperature (Pearce *et al* 1986). Infrared radiation emitted by tissue and that reaches the IR detector originates from a *finite volume* within the tissue. Assuming a 1D geometry, the tissue sample can be divided into infinitely wide slabs of thickness dz . Each slab emits IR radiation that is attenuated as it propagates through overlying tissue slabs towards the tissue surface. By integrating the volume emission (W cm^{-3}) from each slab over the sample thickness (cm), the measured emissive power (W cm^{-2}) is calculated. Since the tissue surface temperature is inferred from the measured emissive power, the estimated surface temperature depends on the temperature distribution within the tissue.

Thus, at any given time the actual surface temperatures of two objects may be identical, but if different superficial temperature gradients exist within each object, the estimated surface temperatures of the two objects will differ substantially. Pearce *et al* (1986) estimated that for typical laser sources, the measured emissive power could be as much as 13.6 times lower than the value that would be measured if the temperature inside the object were uniform and equal to the actual surface temperature. Since radiometric temperature is nonlinearly proportional to measured emissive power, a decay in temperature over the viewing depth of the IR detector will result in an underestimation of the actual surface temperature.

For typical IR imaging bands (3–5 μm and 8–12 μm), if thermal gradients are not significant within approximately the first 100 μm of the surface, then the radiometric temperature will approximate the actual surface temperature. However, for laser irradiation studies involving highly absorbed laser light (e.g. the tissue absorption coefficient μ_a (cm^{-1}) at the laser wavelength is equal to or larger than the average absorption coefficient over the IR detection bandwidth), there will be a discrepancy between the estimated and actual temperatures. If transient temperatures are important, then it may be necessary to correct radiometric temperatures. For example, if radiometric temperature measurements are used (a) to identify threshold temperatures of an event (i.e. photocoagulation of blood (Pfefer *et al* 1999)) or (b) to determine optical and/or thermal properties of an object using pulsed photothermal techniques (Prahl *et al* 1992); then any errors associated with the temperature values obtained radiometrically will result in an inaccurate property calculation.

Limitations of the 1D analytical calculations of Pearce *et al* (1986) include the following: (a) only an exponential decay in the temperature as a function of depth was modelled, and (b) no heat transfer processes that change the shape and amplitude of the temperature distribution were considered. We developed a finite difference model that incorporates heat transfer during and after a laser pulse to heat tissue or a cryogen spurt to cool the surface, any type of temperature distribution (e.g. surface or subsurface temperature peak, etc.), and any band-limit for the IR detector (e.g. 3–5 μm , 8–12 μm).

This paper presents preliminary results of this model, as well as the thermal response of tissue during ablation and cryogen spray cooling (CSC). The implications of the dynamic events that occur during application of laser radiation or CSC on IR temperature measurements are discussed.

2. Basic model

The method of finite differences (Incropera and DeWitt 1996) was applied to the modelling of the thermal response of tissue to laser irradiation and the radiometric temperature measurements with an IR detector. Following is a brief description of the basic features and structure of the model.

2.1. Hardware and software

The program was developed in the MATLAB 5.2 coding environment (The MathWorks, Inc., Natick, MA). The software was run on a 266 MHz Pentium II computer.

2.2. Geometry of tissue

The tissue was modelled in a 1D geometry by dividing the tissue into a finite number of nodes (figure 1). $T_0, T_1, T_2, \dots, T_n$ represented the temperatures of nodes 0, 1, 2, \dots , n . E_0 represented the irradiance (W cm^{-2}) of the incident laser radiation (see section 2.3 below). Each node was of thickness dz , with one exception: the surface node was divided into two half nodes (thickness = $dz/2$), one half representing the adjacent environment, the other the surface layer of the tissue. The initial temperature of the tissue was uniform.

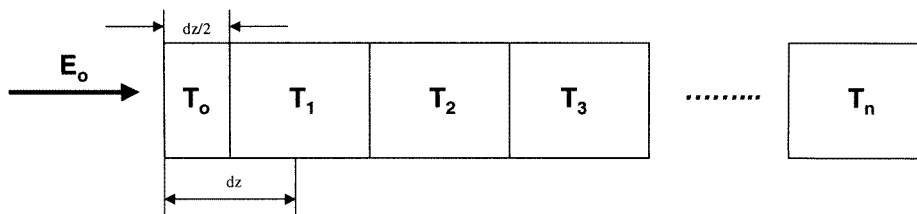


Figure 1. Division of tissue into nodal elements.

For simulations using the basic model, the optical and thermal properties were held constant. The optical properties included the absorption coefficient of the tissue at the wavelength of the incident laser light (μ_a , in cm^{-1}) and an average absorption coefficient of the tissue to the IR radiation that comprised the signal reaching the IR detector (μ_{IR} , in cm^{-1}). The value of the latter parameter depends on the optical bandwidth of the detector and the absorption spectrum of the tissue chromophore that absorbs/attenuates the IR signal. For most soft tissues, water serves as the primary absorber of IR radiation. Previous studies by Prahl *et al* (1992) and Anvari *et al* (1998) have assumed that μ_{IR} is constant for the detection bandwidth they used (3–12 μm and 3–5 μm respectively). However, the absorption spectrum in this wavelength range is not constant (figure 2). Due to the complexities of incorporating this wavelength dependence of the absorption coefficient, we also chose to use a constant value for μ_{IR} : 300 cm^{-1} for 3–5 μm detectors and 792 cm^{-1} for 8–12 μm detectors (Pearce *et al* 1986).

The thermal properties include: density (ρ , in g cm^{-3}), specific heat (c , in $\text{J g}^{-1} \text{ }^\circ\text{C}^{-1}$), thermal conductivity (k , in $\text{W cm}^{-1} \text{ }^\circ\text{C}^{-1}$), and thermal diffusivity ($\alpha = k/\rho c$, in $\text{cm}^2 \text{ s}^{-1}$).

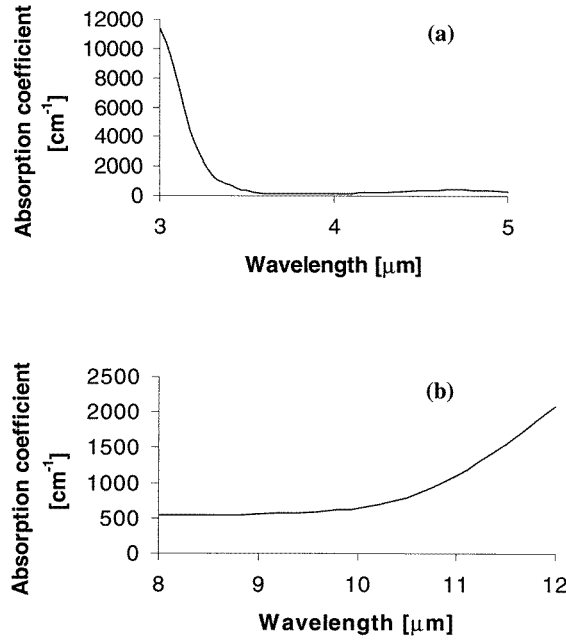


Figure 2. Absorption spectrum of water in the (a) 3–5 μm and (b) 8–12 μm spectral range.

2.3. Source term

The interaction between incident photons and tissue was assumed to be purely absorptive in nature; effects of scattering were not considered. Thus, the optical distribution of the laser light as a function of depth was described using Beer's law:

$$\phi(z) = E_0 \exp(-\mu_a z) \quad (1)$$

where $\phi(z)$ is the fluence rate (W cm^{-2}) at depth z . The corresponding heat generation source term (W cm^{-3}) is

$$S(z) = \mu_a \phi(z). \quad (2)$$

The average source term for each node in the finite difference model was calculated by integration of equation (2) over the corresponding thickness of each node ($dz/2$ for the surface node, dz for all other nodes). The resulting equations for the source term of the surface and internal nodes are, respectively:

$$S_0 = \frac{2E_0}{dz} \left[1 - \exp\left(-\frac{\mu_a dz}{2}\right) \right] \quad (3a)$$

$$S_i = -\frac{E_0 \exp(-\mu_a z)}{dz} \left[\exp\left(-\frac{\mu_a dz}{2}\right) - \exp\left(\frac{\mu_a dz}{2}\right) \right] \quad (3b)$$

where i is the index of each node (e.g. surface node $i = 0$, first interior node $i = 1$, etc).

Since a 1D geometry was used to represent the tissue, the incident laser radiation was modelled as an incoming plane wave since the spot size of the laser was much greater than the $1/e$ penetration depth ($\delta = 1/\mu_a$) of the laser radiation in the tissue. For most of the simulations, the value of μ_a was 594 cm^{-1} , corresponding to the estimated absorption coefficient of CO_2 laser radiation ($\lambda = 10.6 \mu\text{m}$) in a tissue of 70% water content (e.g. skin

(Walsh and Deutsch 1988)). This absorption coefficient corresponded to a penetration depth of $\sim 17 \mu\text{m}$, which is much smaller than the spot size of typical CO_2 laser systems, and so the plane wave assumption is a good approximation for these simulations. For one model, lower absorption coefficients were used, corresponding to those used in a model by Jacques (1993a); the implications will be discussed later.

2.4. Temperature calculations

During each time iteration of the model, the new temperature of each node was calculated using the following equations:

$$T_0^{t+dt} = 2F_0 T_1^t (1 - 2F_0) + S_0 \frac{F_0 (dz)^2}{k} \quad (4a)$$

$$T_i^{t+dt} = F_0 (T_{i-1}^t + T_{i+1}^t) + T_i^t (1 - 2F_0) + S_i \frac{F_0 (dz)^2}{k} \quad (4b)$$

where F_0 is the dimensionless Fourier number ($F_0 = \alpha dt / dz^2$, where dt is the time step between each time iteration), and variables of the form T_i^t represent the temperature of node i at time t .

Since this finite difference model is explicit in nature (e.g. temperatures at time t are dependent only on values from the previous time iteration), it is necessary to check the stability of the model. Explicit finite difference models are not inherently stable; only certain combinations of dt and dz can be used. For equations (4a) and (4b), the stability condition is

$$F_0 < \frac{1}{2}. \quad (5)$$

2.5. Volume emission term corresponding to actual surface temperature

The measured emissive power should equal the value corresponding to the temperature of the surface node T_0 . The first step is to calculate the appropriate wavelength–temperature product corresponding to the bounds of the detector bandwidth; for example, if T_0 is 400 K and the detector bandwidth is 3–5 μm , the wavelength–temperature products at 3 μm and 5 μm are 1200 $\mu\text{m K}$ and 2000 $\mu\text{m K}$ respectively. The fraction f of the total blackbody emissive power ($E_b = \sigma T_0^4$, where $\sigma = 5.67 \times 10^{-12} \text{ W cm}^{-2} \text{ K}^{-4}$ is the Stefan–Boltzmann constant) was determined by using the wavelength–temperature products and the blackbody radiation function table provided by Incropera and DeWitt (1996). Once the band-limited emissive power was determined ($E_{\text{BL}} = f \sigma T_0^4$), the volume emission (W cm^{-3}) for each node was calculated as $E_v = \mu_{\text{IR}} E_{\text{BL}}$.

2.6. Contribution of volume emission terms to IR signal

The IR signal that eventually reaches the detector comprises volume emission terms from a finite volume of tissue. The task of the simulation is to determine the relative contribution of each node to the overall signal. Since radiation in the 3–5 and 8–12 μm bandwidths is well absorbed by water, it is reasonable to assume that attenuation can be described by Beer's law (equation (1)). Thus, the effective volume emission (W cm^{-3}) from each node was determined by using the following equation:

$$E_{v,\text{eff}} = E_v \exp(-\mu_{\text{IR}} z). \quad (6)$$

2.7. Total emissive power

The total emissive power (E_{meas} , in W cm^{-2}) was computed by integrating equation (6) numerically over the entire tissue thickness using the trapezoidal rule (Press *et al* 1988).

2.8. Predicted radiometric temperature measurement for a given timestep

Curves depicting the relationship between emissive power and temperature are shown in figure 3. Calibration equations derived from these curves were used to convert E_{meas} to a radiometric temperature value. A comparison was drawn between the actual surface temperature (T_0) and the radiometric temperature for each timestep.

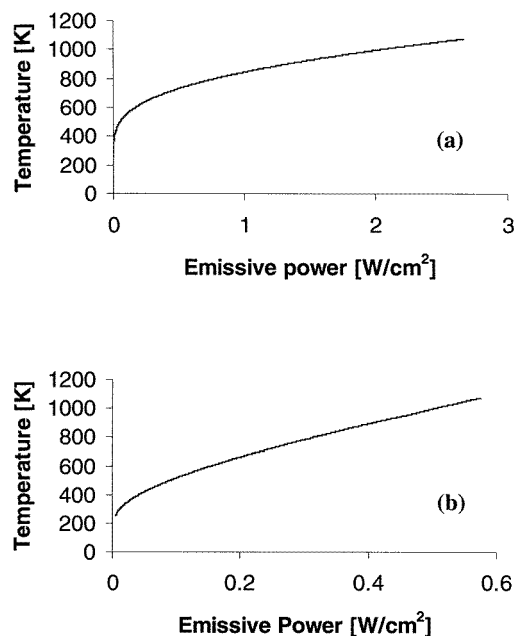


Figure 3. Temperature as a function of emissive power for a detector with a bandwidth of (a) 3–5 μm or (b) 8–12 μm .

3. Incorporation of other models

3.1. Ablation models

The interaction between laser light and tissue is a highly complex process. In tissue with a high water content, the main absorbing chromophore for IR radiation is tissue water. The laser radiation absorbed by tissue water induces a fast temperature rise. If the increased local temperatures are sufficient to cause boiling of the tissue water, then the local pressure will rapidly increase as microbubbles form. The explosive removal of tissue fragments will occur if the mechanical strength of the structural components is inadequate to contain the expanding vapour bubble.

Several papers have been published on the topic of tissue ablation (Cummings and Walsh 1992, 1993, Green *et al* 1990, Hibst and Kaufmann 1991a, b, Izatt *et al* 1990a, b, Jacques

1993b, Jansen *et al* 1993, Kaufmann and Hibst 1996, LeCarpentier *et al* 1993, Oraevsky *et al* 1996, Partovi *et al* 1987, Rastegar *et al* 1989, Sagi *et al* 1992, Sathyam *et al* 1996, van Leeuwen *et al* 1995, Verdaasdonk *et al* 1990, Walsh and Deutsch 1988, Walsh *et al* 1988, Welch *et al* 1991). However, modelling the ablation process is extremely difficult due to the large number of parameters that must be considered; the relative role of different variables is still not completely understood.

Nevertheless, three ablation models (Partovi *et al* 1987, Sagi *et al* 1992, Jacques 1993a) were taken from the literature and incorporated in the basic model described in section 2. Although each of the models only considers various aspects of the ablation process, the dynamic events integral to each model presents a more realistic view of the temperature–time history in tissue than our basic model, which does not incorporate tissue ablation or changes in optothermal properties.

A brief description of each model is presented below; for more information, the reader is directed to the original references.

3.1.1. Ablation at 100 °C (Partovi et al 1987). This model assumed that ablation occurred at the boiling temperature of water at atmospheric pressure. Similar to our basic model, the optical and thermal properties were constant during the simulation. During laser irradiation, the temperature of each node was allowed to increase until a value of 100 °C was reached. Once this occurred, the temperature of the node was clamped at 100 °C; any additionally deposited energy supplied the necessary latent heat of vaporization (assumed to be 2250 J cm⁻³) of the tissue water in the node. Once the total latent heat was provided, the node was considered to be ablated.

3.1.2. Ablation at a constant temperature (Sagi et al 1992). Three stages were considered in this numerical model. The first stage involved inducing a temperature rise to an arbitrary boiling temperature of water; we used 100 °C. During this stage, the optical and thermal properties were held constant. Once the boiling temperature was reached for a given node, the second stage began in which the temperature was clamped at the boiling value while the latent heat of vaporization (2250 J cm⁻³) was supplied. In this stage, the water content of the node decreased due to the boiling process. The thermal properties were assumed to be dependent on water content, and so they also changed during the second stage. The third stage began when the total latent heat was supplied for a given node. The thermal properties were held constant, and the temperature of the node increased until it reached an arbitrary ablation temperature, at which the node was removed. For these simulations, we used 330 °C as the ablation temperature.

3.1.3. Cyclic ablation process (Jacques 1993a). Jacques implemented a 1D finite difference model to simulate tissue ablation. However, instead of calculating new temperatures during each time step, he determined the energy deposition (J cm⁻³). Since our prediction of radiometric temperature measurements was dependent on a known temperature distribution in the tissue, the energy deposition term for each node was converted to a temperature value using the following approximation:

$$T_i = T_{\text{init}} + \frac{Q_i}{\rho c} \quad (7)$$

where T_{init} is the initial temperature (°C) and Q_i is the heat storage term of the node at index i .

During a given timestep, a new Q_i was calculated for each node. For a given node, if the value of Q_i was greater than a threshold evaporation value ($Q_{\text{evap}} = 418 \text{ J cm}^{-3}$,

or about 130 °C), then water evaporation was initiated. As the water content of a node changed, its thermal properties also changed because they were considered to be dependent on water content. Two novel features of this model included: (a) consideration of water diffusion along a concentration gradient, and (b) implementation of tissue charring. The latter occurred when the term Q_i reached a value larger than a threshold energy deposition term Q_{char} , which was equal to 800 J cm⁻³ (~225 °C). After this value of Q_i was reached, the absorption coefficient of the node increased at a constant rate (333 cm⁻¹ s⁻¹) until a maximum value of 67 cm⁻¹ was attained, to simulate the higher absorption of char (Jacques 1993b).

Once an energy deposition value of 1500 J cm⁻³ was reached for a given node, the node was considered to be ablated. Since this node may be subsurface, all nodes above this node were also removed from the tissue; explosive removal of tissue was considered. Since the new surface node was now exposed to atmospheric conditions, its parameters were set to $T = 130$ °C and $Q_i = 418$ J cm⁻³. This process was allowed to continue during the entire simulation.

During adaptation of this model to our basic model, all laser and tissue parameters were taken directly from the paper by Jacques (1993a). For his model, an 805 nm diode laser was the light source and was assumed to produce a 2 mm diameter flattop laser spot. The tissue model consisted of a non-scattering medium stained superficially (100 μm deep) by indocyanine green (ICG). The absorption coefficients of the ICG-stained tissue and the unstained tissue were 10 cm⁻¹ and 0.1 cm⁻¹ respectively; these values correspond to penetration depths of 100 μm and 10 mm respectively. Thus, the penetration depth of the laser light in the unstained tissue is larger than the spot size, and so the uniform plane wave assumption is suspect. However, since only 37% of the laser light was incident on the unstained tissue layer, and because the uniform plane wave assumption was valid for the ICG-stained layer, the 1D geometry of the model was deemed satisfactory for this irradiation scenario.

3.2. Cryogen cooling

A fourth feature was implemented in our basic model and used to study the effects of CSC on skin. The experimental conditions proposed by Anvari *et al* (1998) were used. Briefly, the interaction between cryogen spray and skin was modelled as a convective boundary condition. The environmental temperature was set at $T_{\infty} = -7$ °C, and the effective convection heat transfer coefficient was $h = 4$ W cm⁻² K⁻¹. During the spurt, ice formation occurred on the surface of the skin. The ice was modelled as a layer of finite thickness and infinite extent, and it formed at a rate of 0.1 cm s⁻¹ during the spurt. Similar to the Anvari *et al* model, heat transfer involving this ice layer was not considered, and the convective boundary condition was maintained even after ice formation had begun. The ice layer contributed to attenuation of the emitted IR signal because of its high absorptive properties in the infrared. To simplify the model, we assumed that $\mu_{\text{IR,tissue}} \approx \mu_{\text{IR,ice}}$; thus, the ice absorption coefficient was 300 cm⁻¹ and 792 cm⁻¹ for detection bandwidths of 3–5 μm and 8–12 μm respectively. The former ice absorption coefficient was less than the 400–600 cm⁻¹ range of absorption coefficients used by Anvari *et al*; however, this discrepancy was not expected to qualitatively affect our results on the relationship between the actual and radiometric surface temperatures.

4. Description of simulations

4.1. Constant temperature

To test the basic model, simulations were run in which the tissue temperature was fixed at a constant value throughout the tissue. Since no thermal gradients were present, the radiometric temperature estimation predicted by the model was expected to be equal to the tissue temperature. Two simulations were run, one at a tissue temperature of 32 °C, the other at 600 °C. The predicted radiometric temperatures were 32 °C and 602 °C respectively. The close match (within 1%) between the radiometric and tissue temperatures for each case demonstrated the accuracy of the software.

4.1.1. Case 1: basic model—high μ_a . Two cases were examined with the basic model: high-absorption and relatively low absorption of incident laser light. The high absorption case mimicked pulsed CO₂ laser irradiation of skin. The optical and thermal parameters that were used are compiled in table 1. The results of this model were compared with those obtained from cases 3 and 4; the parameters were kept as constant as possible among the three situations. For case 4, the thermal properties of the tissue were different because they were calculated from equations in the reference by Sagi *et al* (1992), whereas the values for cases 1 and 3 were chosen arbitrarily.

Table 1. Optical and thermal properties used in each simulation (cases 1–6). See text for a more detailed description of each case.

	1	2	3	4	5	6
Detector bandwidth	3–5	8–12	3–5	3–5	8–12	8–12
Laser wavelength (nm)	10 600	805	10 600	10 600	805	N/A
μ_{IR} (cm ⁻¹)	300	792	300	300	792	792
μ_a (cm ⁻¹)	594	10	594	594	10, 0.1	N/A
H_0 (J cm ⁻²)	4.95	70.7	4.95	4.95	1590	N/A
Pulse duration	100 μ s	1 s	100 μ s	100 μ s	5 s	N/A
k (W cm ⁻¹ K ⁻¹)	3.70×10^{-3}	3.70×10^{-3}	4.17×10^{-3}	3.70×10^{-3}	4.96×10^{-3}	4.50×10^{-3}
ρ (g cm ⁻³)	1	1	1.035	1	1.045	1
c (J g ⁻¹ K ⁻¹)	4.18	4.18	4.457	4.18	3.82	4.18
T_{init} (°C)	32	32	32	32	25	30

4.1.2. Case 2: basic model—low μ_a . This simulation modelled the use of an 805 nm diode laser on an absorbing medium; the experimental conditions are similar to those used by Jacques (1993a). The operating parameters are listed in table 1.

4.1.3. Case 3: ablation model—ablation at 100 °C. The basic model was altered by using the ablation analysis derived by Partovi *et al* (1987). The simulation emulated one pulse of CO₂ laser radiation applied to skin. Variables of interest are tabulated in table 1.

4.1.4. Case 4: ablation model—ablation at a constant temperature. The model by Sagi *et al* (1992) was incorporated into the basic model. Similar to cases 1 and 3, this model was designed to portray pulsed CO₂ laser radiation on skin. The optical and thermal properties are provided in table 1. Note that the thermal properties (k , c and ρ) listed in the table are those

for fully hydrated skin (as calculated from the equations listed by Sagi *et al*), and that these values changed for nodes undergoing boiling of tissue water.

4.1.5. Case 5: ablation model—cyclic ablation process. The ablation algorithm presented by Jacques (1993a) was added to the basic model. The operating parameters were chosen to be similar to those used by Jacques and are summarized in table 1. The simulation involved irradiation of a medium stained superficially by ICG with an 805 nm diode laser. Similar to case 4, the thermal properties given in the table were dependent on the water content of each node and thus represented initial values.

4.1.6. Case 6: CSC model. The thermal effects of cryogen cooling were simulated using the technique described in the paper by Anvari *et al* (1998). No laser irradiation was considered in this model. Two temperatures were used for the ice that formed on the surface (see above): 0°C and -7°C. The pertinent thermal properties are listed in table 1.

4.2. Assumptions and limitations of the model

- (a) Although the 1D geometry was a reasonable approach to model the tissue (since $\delta \ll$ laser spot size), heat conduction occurred to a minor extent in the radial direction; only axial heat transfer was considered in these simulations.
- (b) The entire IR signal generated from the tissue volume was assumed to reach the detector. Absorption of the emitted radiation by the environment was not considered.
- (c) The responsivity of the IR detector was assumed to be uniform across its bandwidth. For photon detectors, the responsivity is not constant as a function of wavelength, and so wavelength-dependent emission would need to be considered during conversion from emissive power to radiometric temperature.
- (d) μ_{IR} was assumed to be a constant value. The IR regions typically used for detection are 3–5 μm and 8–12 μm . Assuming that water is the primary absorbing chromophore of the target object for the generated IR signal, μ_{IR} is approximately the value for water. However, the absorption spectrum of water in these wavelength ranges varies over several orders of magnitude (Hale and Querry 1973). Also, the absorption coefficient of water has been shown experimentally to have a temperature dependence (Jansen *et al* 1994, Marechal 1991, Walsh and Cummings 1994). Thus, determination of the IR signal reaching the detector should include the wavelength and temperature dependence of the absorption coefficient; modelling μ_{IR} as a constant was performed as a first approximation to the solution of the problem.

5. Results

Note that the term ‘actual surface temperature’ represents the value *at the surface node of the tissue*, even when ice formation occurred during a cryogen spurt (see case 6 below).

5.1. Case 1: basic model—high μ_a

The results of this simulation (figure 4) showed that the actual surface temperature (i.e. the temperature at the surface node) was greatly underestimated by the predicted measurement from the infrared detector.

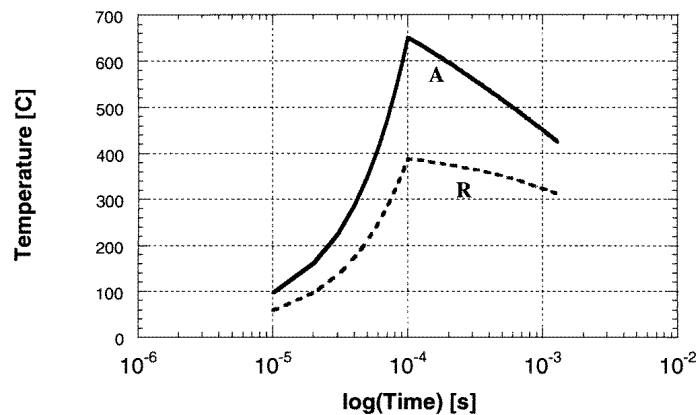


Figure 4. (Case 1) Semilog plot of temperature–time history for a simulated 100 μs CO_2 laser pulse on skin. The predicted radiometric surface temperatures (R, broken curve) were much less (maximum error = 40%) than the actual surface temperatures (A, full curve). $\mu_a = 594 \text{ cm}^{-1}$, $\mu_{\text{IR}} = 300 \text{ cm}^{-1}$.

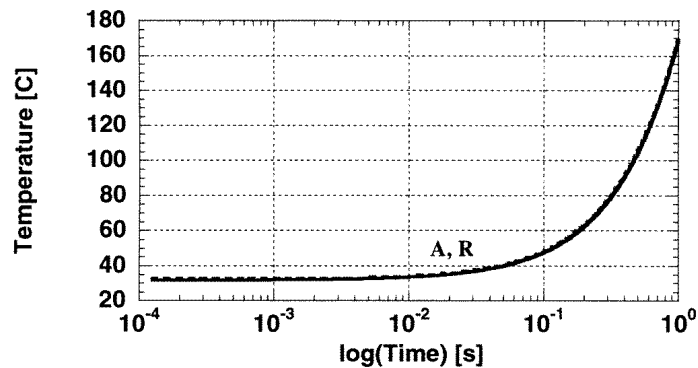


Figure 5. (Case 2) Semilog plot of temperature–time history for a simulated one-second-long 805 nm diode laser pulse on an absorbing medium. The radiometric (R, broken curve) and actual surface (A, full curve) temperatures were approximately the same (maximum error = 4%). $\mu_a = 10 \text{ cm}^{-1}$, $\mu_{\text{IR}} = 792 \text{ cm}^{-1}$.

5.2. Case 2: basic model—low μ_a

The radiometric and actual surface temperatures were almost identical to one another (figure 5).

5.3. Case 3: ablation model—ablation at 100°C

Due to a constraint imposed in the model by Partovi *et al* (1987), the maximum temperature of any node was 100°C; since ablation also occurs at 100°C, it is not readily apparent that tissue removal is occurring when interpreting the temperature–time history (figure 6). The predicted radiometric temperatures were less than the actual surface temperatures due to the superficial thermal gradient induced by the laser pulse.

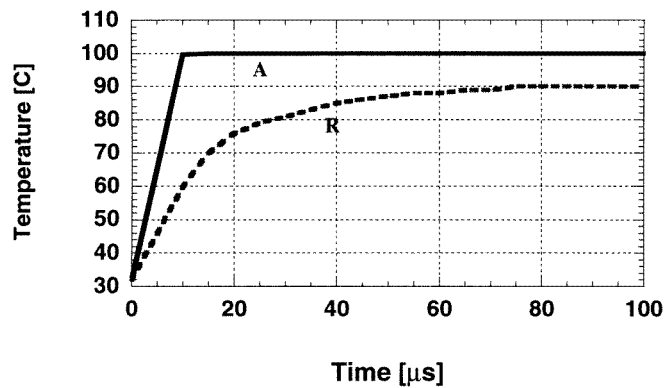


Figure 6. (Case 3) Temperature–time history for a simulated 100 μs CO_2 laser pulse on skin. The ablation model by Partovi *et al* (1987) was incorporated into our basic model. The maximum temperature of 100 $^\circ\text{C}$ was reached within the first 10 μs of laser irradiation. The predicted radiometric temperature measurement (R, broken curve) was less (maximum error = 40%) than the actual surface temperature (A, full curve) throughout the duration of this simulation. $\mu_a = 594 \text{ cm}^{-1}$, $\mu_{\text{IR}} = 300 \text{ cm}^{-1}$.

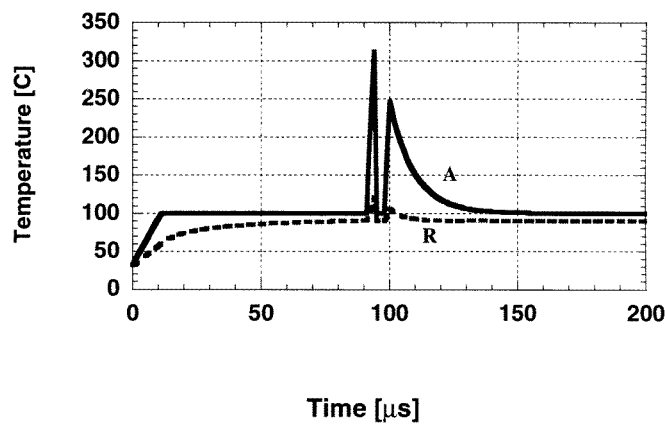


Figure 7. (Case 4) Temperature–time history for a simulated 100 μs CO_2 laser pulse on skin. The ablation model by Sagi *et al* (1992) was incorporated into our basic model. Ablation occurred at $t = 94 \mu\text{s}$. The predicted radiometric temperature measurement (R, broken curve) was less (maximum error = 61%) than the actual surface temperature (A, full curve) throughout the duration of this simulation. $\mu_a = 594 \text{ cm}^{-1}$, $\mu_{\text{IR}} = 300 \text{ cm}^{-1}$.

5.4. Case 4: ablation model—ablation at a constant temperature

The shape of the radiometric temperature curve closely followed that of the actual surface temperature lineshape (figure 7), but the amplitude of the former was less at all time steps. This underestimation was largest at $t = 94 \mu\text{s}$, corresponding to a time at which tissue ablation occurred.

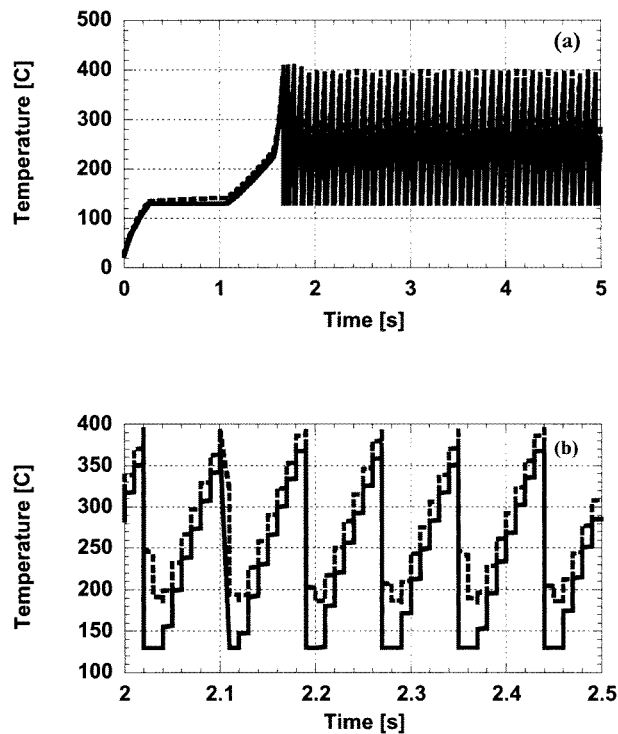


Figure 8. (Case 5) Simulated temperature response to irradiation with an 805 nm diode laser. The cull curve shows the actual surface temperature, and the broken curve the predicted radiometric temperature. (a) Total run time of simulation. Note the oscillating temperatures at $t > 1.6$ s that were due to the inherent nature of the ablation model by Jacques (1993a) (see text for more details). (b) Temperature–time history between 2 and 2.5 s. Note that the radiometric temperatures (broken curve) are greater than the actual surface temperature (full curve).

5.5. Case 5: ablation model—cyclic ablation process

The thermal response of the medium to 805 nm laser irradiation is shown in figure 8. Once ablation was initiated ($t = 1.6$ s, see figure 8(a)), a temperature cycle began in which (a) the new surface node was set at $T = 130^\circ\text{C}$, (b) the temperature was allowed to increase and (c) explosive removal of tissue occurred as soon as any node reached the ablation threshold. During this cyclic ablation process, the radiometric temperature was *greater* than the actual surface temperature (figure 8(b)). This was due to the presence of a subsurface temperature peak; when ablation occurred, the new surface was set at $T = 130^\circ\text{C}$, but the temperatures of the immediate subsurface nodes were greater than this value. The contribution of these nodes to the IR signal reaching the detector resulted in a radiometric temperature that was larger than the actual surface temperature.

5.6. Case 6: CSC model

The thermal response of skin to CSC was simulated by implementing the model proposed by Anvari *et al* (1998). The effects of a 100 ms cryogen spurt on skin were modelled, and two ice temperatures were considered: 0°C (figure 9(a)) and -7°C (figure 9(b)). In both plots, the temperature response of the surface node over time was the same (full curve). When the

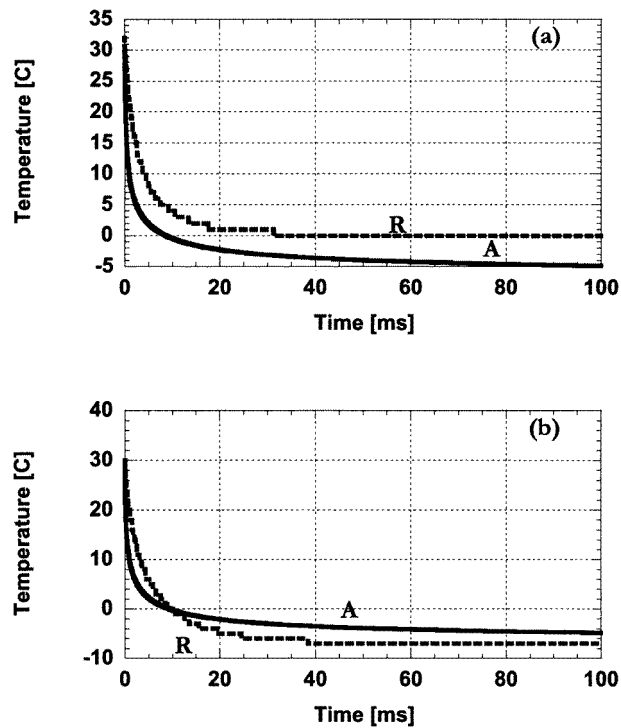


Figure 9. (Case 6) Simulated thermal response of skin to a 100 ms cryogen spurt. The full curve shows the actual surface temperature, and the broken curve the radiometric temperature. The ice which formed on the surface (see text) was set at (a) 0°C and (b) -7°C . The temperature–time history of the surface node was identical for both cases. The predicted radiometric temperature measurements were very different for the two scenarios.

ice temperature was set at 0°C , the radiometric temperature measurement was greater than the actual surface temperature during the entire cryogen spurt. When the ice was set at -7°C , the radiometric temperatures were initially greater than the temperature of the surface node (figure 9(b)). At $t = 10$ ms, the radiometric and actual surface temperatures were equal, after which the radiometric values were less than the surface temperatures.

6. Discussion

In this paper, only blackbody emission was considered; in reality, tissue is not an ideal blackbody emitter. Complete consideration of the wavelength and directionality dependence of emissivity ε is beyond the scope of this report. If emissivity were assumed to be constant over the infrared detector bandwidth and independent of direction (limitation of 1D model), then $\varepsilon(\lambda, \theta)$ would reduce to a constant value that would be a simple multiplicative factor when the total emissive power is calculated. If calculation of the radiometric temperature were done under the auspice of blackbody emission, and the tissue was in reality a non-ideal emitter, then a nonlinear reduction in the radiometric temperature measurement would occur (figure 3).

The results of these simulations (figures 4–9) demonstrate one important feature in using IR detectors for surface temperature measurements. Laser light that is highly absorbed in a medium will induce a steep temperature gradient within the superficial layers. Since IR

radiometers receive thermal emission from a *finite* 'viewing depth' within an object, surface temperature estimations will be erroneous if the thermal gradient is significant within this region.

The relationship between radiometric and actual surface temperatures can be presented as three general cases. For these examples, the position of the thermal gradients is related to the detector 'viewing depth'. Although the use of such a term is an oversimplification of the detection process, it is useful for describing the trends among the temperature values. Let us assume that the viewing depth of a detector is $100\ \mu\text{m}$, and consider the following situations:

- (a) *Peak temperature at surface, sharp temperature decrease within viewing depth*: this situation occurs when the tissue absorption coefficient is high for the incident radiation. The resulting radiometric temperature underestimates the actual surface temperature. Examples: cases 1 (figure 4), 3 (figure 6) and 4 (figure 7).
- (b) *Small or no significant temperature gradient within viewing depth*: this event can be the result of very low absorption of the incident laser light. The radiometric temperature estimate should be nearly equal to the true surface value. Example: case 2 (figure 5).
- (c) *Subsurface temperature peak within detector viewing depth*: surface cooling can induce such a temperature distribution. The radiometric temperature overestimates the actual surface value. Examples: cases 5 (figure 8(b)) and 6 (figure 9(a)).

Implementation of the ablation model by Jacques (1993a) resulted in subsurface temperature peaks during the cyclic ablation process, whereas the other two ablation models (Partovi *et al* 1987, Sagi *et al* 1992) predicted surface temperature peaks. The effects of this difference on the predicted radiometric temperatures were an overestimation and underestimation, respectively, of the true surface value. The lack of a satisfying description of the true dynamics of tissue ablation precludes us from a critical analysis of the three ablation models. According to the results of our model (figures 6–8), the actual events that take place during high-power laser irradiation of tissue are important for determining whether the estimated radiometric temperature is greater or less than the actual surface temperature.

The different results obtained from the CSC model were due to the two temperatures attributed to the ice that formed during the cryogen spurt. When ice formation was set at 0°C (figure 9(a)), the radiometric temperature was always greater than the true surface temperature. The latter value reached 0°C approximately 10 ms into the cryogen spurt and continued to decrease. For $t < 10$ ms, the thickness of the ice layer was less than $1\ \mu\text{m}$, and so the temperature of the ice layer did not significantly alter the radiometric temperatures during the first 10 ms. Thus, since the true surface temperature at $t > 10$ ms decreased to temperatures less than 0°C , and because the minimum radiometric temperature was equal to the ice temperature of 0°C , the radiometric temperature was greater than the actual surface value for the remainder of the cryogen spurt.

For an ice formation temperature of -7°C (figure 9(b)), the radiometric temperatures were greater than the actual surface temperature during the first 10 ms of the spurt. However, since the ice temperature was much lower than the temperatures within the tissue, the calculated radiometric value decreased below the true surface temperature. For $t > 10$ ms, the surface temperature slowly approached the cryogen temperature of -7°C , while the increasing ice layer thickness induced a faster convergence of the radiometric temperatures to the ice temperature.

7. Conclusions

With the aid of numerical modelling, we have shown that infrared temperature measurements during laser irradiation or cryogen cooling of an object can be significantly different from the actual surface temperature. This can have a large effect on the use of temperature feedback to ascertain threshold temperatures or determine optical and thermal properties. If the measured temperature is not approximately equal to the actual surface temperature, then error propagation will result in inaccurate estimates of these parameters.

Acknowledgments

The authors thank Drs Tom Milner and Josh Pfefer for invaluable discussions and comments. The research was supported by the Office of Naval Research Medical Free Electron Laser Biomedical Science Program (N0014-91-J1564), the Albert W and Clemmie A Caster Foundation, and the Air Force Office of Scientific Research through MURI from DDR&E (F49620-98-1-0480).

References

- Anvari B, Milner T E, Tanenbaum B S and Nelson J S 1998 A comparative study of human skin thermal response to sapphire contact and cryogen spray cooling *IEEE Trans. Biomed. Eng.* **45** 934–41
- Cummings J P and Walsh J T 1992 Q-switched laser ablation of tissue: plume dynamics and the effect of tissue mechanical properties *Proc. SPIE* **1646** 242–53
- 1993 Tissue tearing caused by pulsed laser-induced ablation pressure *Appl. Opt.* **32** 494–503
- Green H A, Domankevitz Y and Nishioka N S 1990 Pulsed carbon dioxide laser ablation of burned skin: *in vitro* and *in vivo* analysis *Lasers Surg. Med.* **10** 476–84
- Hale G M and Querry M R 1973 Optical constants of water in the 200 nm to 200 μm region *Appl. Opt.* **12** 555–63
- Hibst R and Kaufmann R 1991a Fundamentals of pulsed UV and mid-infrared laser skin ablation *Lasers in Dermatology* ed R Steiner, R Kaufmann, M Landthaler and O Braun-Falco (Berlin: Springer) pp 102–15
- 1991b Effects of laser parameters on pulsed Er-YAG laser skin ablation *Lasers Med. Sci.* **6** 391–7
- Incropera F P and DeWitt D P 1996 *Fundamentals of Heat and Mass Transfer* (New York: Wiley)
- Izatt J A, Albagli D, Itzkan I and Feld M S 1990b Pulsed laser ablation of calcified tissue: Physical mechanisms and fundamental parameters *Proc. SPIE* **1202** 133–40
- Izatt J A, Sankey N D, Partovi F, Fitzmaurice M, Rava R P, Itzkan I and Feld M S 1990a Ablation of calcified biological tissue using pulsed hydrogen fluoride laser radiation *IEEE J. Quantum Electron.* **26** 2261–70
- Jacques S L 1993a Finite-difference modelling of laser ablation of tissue *Proc. SPIE* **1882** 422–31
- 1993b Role of tissue optics and pulse duration on tissue effects during high-power laser irradiation *Appl. Opt.* **32** 2447–54
- Jansen E D, Le T H and Welch A J 1993 Excimer, Ho:YAG, and Q-switched Ho:YAG ablation of aorta: a comparison of temperatures and tissue damage *in vitro Appl. Opt.* **32** 526–34
- Jansen E D, van Leeuwen T G, Motamedi M, Borst C and Welch A J 1994 Temperature dependence of the absorption coefficient of water for midinfrared laser radiation *Lasers Surg. Med.* **14** 258–68
- Kaufmann R and Hibst R 1996 Pulsed erbium: YAG laser ablation in cutaneous surgery *Lasers Surg. Med.* **19** 324–30
- LeCarpentier G L, Motamedi M, McMath L P, Rastegar S and Welch A J 1993 Continuous wave laser ablation of tissue: analysis of thermal and mechanical events *IEEE Trans. Biomed. Eng.* **40** 188–200
- Marechal Y 1991 Infrared spectra of water. I. Effect of temperature and of H/D isotopic dilution *J. Chem. Phys.* **95** 5565–73
- Oraevsky A A, Jacques S L, Esenaliev R O and Tittel F K 1996 Pulsed laser ablation of soft tissues, gels and aqueous solutions at temperatures below 100 °C *Lasers Surg. Med.* **18** 231–40
- Partovi F, Izatt J A, Cothren R M, Kittrell C, Thomas J E, Strikwerda S, Kramer J R and Feld M S 1987 A model for thermal ablation of biological tissue using laser radiation *Lasers Surg. Med.* **7** 141–54
- Pearce J A, Welch A J, Motamedi M and Agah R 1986 Thermographic measurement of tissue temperature during laser angioplasty *Heat and Mass Transfer in the Microcirculation of Thermally Significant Vessels* ed K R Diller and R B Roemer (New York: ASME) pp 49–54

- Pfefer T J, Choi B, Vargas G, McNally K M and Welch A J 1999 Mechanisms of laser-induced thermal coagulation of whole blood *in vitro* *Proc. SPIE* **3590** 20–31
- Prahl S A, Vitkin I A, Bruggemann U, Wilson B C and Anderson R R 1992 Determination of optical properties of turbid media using pulsed photothermal radiometry *Phys. Med. Biol.* **37** 1203–17
- Press W H, Flannery B P, Teukolsky S A and Vetterling W T 1988 *Numerical Recipes in C* (Cambridge: Cambridge University Press)
- Rastegar S, Motamedi M, Welch A J and Hayes L J 1989 A theoretical study of the effect of optical properties in laser ablation of tissue *IEEE Trans. Biomed. Eng.* **36** 1180–7
- Sagi A, Avidor-Zehavi A, Shitzer A, Gerstmann M, Akselrod S and Katzir A 1992 Heating of biological tissue by laser irradiation: temperature distribution during laser ablation *Opt. Eng.* **31** 1425–31
- Sathyam U S, Shearin A and Prahl S A 1996 Visualization of microsecond laser ablation of porcine clot and gelatin under a clear liquid *Proc. SPIE* **2681** 28–35
- Small W, Celliers P M, Da Silva L B, Matthews D L and Soltz B A 1997 Two-color infrared thermometer for low-temperature measurement using a hollow glass optical fiber *Proc. SPIE* **2977** 115–20
- Torres J H, Ghaffari S and Welch A J 1990a Laser probe temperature control by measuring the returning infra-red radiation *Med. Biol. Eng. Comput.* **28** 1–7
- Torres J H, Motamedi M and Welch A J 1990b Disparate absorption of argon laser radiation by fibrous versus fatty plaque: implications for laser angioplasty *Lasers Surg. Med.* **10** 149–57
- Torres J H, Springer T A, Welch A J and Pearce J A 1990c Limitations of a thermal camera in measuring surface temperature of laser-irradiated tissues *Lasers Surg. Med.* **10** 510–23
- Valvano J W and Pearce J 1995 Temperature measurements *Optical-Thermal Response of Laser-Irradiated Tissue* ed A J Welch and M J C van Gemert (New York: Plenum) pp 489–534
- van Leeuwen T G, Jansen E D, Motamedi M, Borst C and Welch A J 1995 Pulsed laser ablation of soft tissue *Optical-Thermal Response of Laser-Irradiated Tissue* ed A J Welch and M J C van Gemert (New York: Plenum) pp 709–63
- Verdaasdonk R M, Borst C and van Gemert M J C 1990 Explosive onset of continuous wave tissue ablation *Phys. Med. Biol.* **35** 1129–44
- Walsh J T and Cummings J P 1994 Effect of the dynamic optical properties of water on midinfrared laser ablation *Lasers Surg. Med.* **15** 295–305
- Walsh J T and Deutsch T F 1988 Pulsed CO₂ laser tissue ablation: measurement of the ablation rate *Lasers Surg. Med.* **8** 264–75
- Walsh J T, Flotte T J, Anderson R R and Deutsch T F 1988 Pulsed CO₂ laser tissue ablation: effect of tissue type and pulse duration on thermal damage *Lasers Surg. Med.* **8** 108–18
- Welch A J, Bradley A B, Torres J H, Motamedi M, Ghidoni J J, Pearce J A, Hussein H and O'Rourke R A 1987 Laser probe ablation of normal and atherosclerotic human aorta *in vitro*: a first thermographic and histologic analysis *Circulation* **76** 1353–63
- Welch A J, Motamedi M, Rastegar S, LeCarpentier G L and Jansen D 1991 Laser thermal ablation *Photochem. Photobiol.* **53** 815–23